

Article

Effects of Tin and Sulfur Chemical Substitution on the Structural and Electrical Properties of CuCr_2Se_4 Selenospinel

 Paulina Valencia-Gálvez ¹, Daniel Aravena ², Patricia Barahona ³, Silvana Moris ^{4,*} and Antonio Galdámez ^{1,*}
¹ Departamento de Química, Facultad de Ciencias, Universidad de Chile, Las Palmeras 3425, Chile; paulygav@uchile.cl

² Departamento de Química de los Materiales, Facultad de Química y Biología, Universidad de Santiago de Chile, Casilla 40, Correo 33, Santiago 9170022, Chile; daniel.aravena.p@usach.cl

³ Facultad de Ciencias Básicas, Universidad Católica del Maule, Avenida San Miguel 3605, Talca 3480112, Chile; pbaraho@ucm.cl

⁴ Centro de Investigación de Estudios Avanzados del Maule (CIEAM), Vicerrectoría de Investigación y Postgrado, Universidad Católica del Maule, Avenida San Miguel 3605, Talca 3480112, Chile

* Correspondence: smoris@ucm.cl (S.M.); agaldamez@uchile.cl (A.G.)

Abstract: A series of $\text{CuCr}_{2-x}\text{Sn}_x\text{S}_{2.3}\text{Se}_{1.7}$ and $\text{CuCr}_{2-x}\text{Sn}_x\text{S}_{1.7}\text{Se}_{2.3}$ ($x = 0.4, 0.6,$ and 1.0) compounds were prepared by solid-state reaction at a high temperature. Single-crystal X-ray diffraction analysis showed that $\text{CuCr}_{1.1}\text{Sn}_{0.9}\text{S}_{2.3}\text{Se}_{1.7}$ crystallizes in a spinel-type structure (cubic $Fd\bar{3}m$ space group). The others samples were also consistent with a spinel-type structure but through powder X-ray diffraction patterns and Rietveld refinements. The systems studies showed *p*-type semiconductor behavior with a carrier concentration per volume of approximately $\sim +10^{20} \text{ cm}^{-3}$. The electrical conductivity, σ , showed tin-content dependence. The conductivity of $\text{CuCr}_{2-x}\text{Sn}_x\text{S}_{1.7}\text{Se}_{2.3}$ increased from ~ 9.0 to $\sim 17.0 \text{ S}\cdot\text{cm}^{-1}$ at room temperature (RT) for $x = 0.4$ and 0.6 , respectively, and the magneto-resistance average value determined for $\text{CuCr}_{2-x}\text{Sn}_x\text{S}_{2.3}\text{Se}_{1.7}$ and $\text{CuCr}_{2-x}\text{Sn}_x\text{S}_{1.7}\text{Se}_{2.3}$ was approximately $\sim 10^{-4} \Omega$ (0.566 T , external magnetic field). DFT calculations revealed that the Cr centers concentrated most of the spin density. A smaller spin polarization featuring the opposite spin was observed for S/Se atoms.

Keywords: thio- and selenospinel; electrical properties; single-crystal X-ray diffraction



Citation: Valencia-Gálvez, P.; Aravena, D.; Barahona, P.; Moris, S.; Galdámez, A. Effects of Tin and Sulfur Chemical Substitution on the Structural and Electrical Properties of CuCr_2Se_4 Selenospinel. *Appl. Sci.* **2022**, *12*, 1586. <https://doi.org/10.3390/app12031586>

Academic Editor: Bertrand Lenoir

Received: 22 December 2021

Accepted: 31 January 2022

Published: 1 February 2022

Publisher's Note: MDPI stays neutral with regard to jurisdictional claims in published maps and institutional affiliations.



Copyright: © 2022 by the authors. Licensee MDPI, Basel, Switzerland. This article is an open access article distributed under the terms and conditions of the Creative Commons Attribution (CC BY) license (<https://creativecommons.org/licenses/by/4.0/>).

1. Introduction

The magnetic and transport properties of AB_2X_4 chalcogenide spinels are strongly influenced by the distribution of the metal ions in the structure. Because the cationic and anionic distribution can change when substitution occurs, the physical properties of the spinel material may differ significantly from those of the parent spinels. An interesting property of spinels containing Cr is magnetoresistance, which refers to the change in the electrical resistance of materials in the presence of a magnetic field [1]. This has been the focus of many studies because of its potential for use in new data storage devices with reduced energy consumption [2,3]. Therefore, solid solutions of seleno- and thiospinels have been well studied because of their extraordinary electrical and magnetic properties, which can differ significantly by substitution [4–11]. For example, replacing metal ions in the octahedral or tetrahedral position with diamagnetic ions can alter the magnetic properties of CuCr_2S_4 and CuCr_2Se_4 . In $(\text{Cu})_{\text{tet}}[\text{Cr}_{2-x}\text{M}_x]_{\text{oct}}\text{Se}_4$ spinels, the substitutions of Cr by M ($\text{M} = \text{Zr}, \text{Sn}$) have indicated that M is present as a 4^+ ion, and Cu as a diamagnetic Cu^+ ion [3,12]. For CuCr_2S_4 , its physical properties can be understood if its charge distribution is assumed to be $\text{Cu}^+\text{Cr}^{3+}\text{Cr}^{4+}\text{S}_4^{8-}$; thus, metallic conduction and ferromagnetism are ascribed to the double exchange between Cr^{3+} and Cr^{4+} [13,14]. Looking at the magnetic phase diagram of $(\text{Cu})_{\text{tet}}[\text{Cr}_{2-x}\text{Ti}_x]_{\text{oct}}\text{S}_4$ [15], which results from the substitution of Cr by Ti, the magnetic frustration generated changes the ferromagnetic properties to a spin-glass

regime. Regarding $(\text{Cu})_{\text{tet}}[\text{Cr}_{2-x}\text{Sn}_x]_{\text{oct}}\text{Se}_4$, where Sn replaced Cr, ferromagnetic interaction at $x = 0.3$ was noticeable, and for $x = 0.7$, ferromagnetic character was predominantly present in the antiferromagnetic (AF) behavior [6]. The degree of Se, Cu, or Cr substitution can modify the magnetic and electrical properties of chalcospinels. For example, $\text{CuCr}_{2-x}\text{Sn}_x\text{S}_2\text{Se}_2$ samples with $x = 0.2$ and 0.4 showed ferromagnetic interaction, whereas high transition temperature (AF) behavior occurred in $x = 0.6, 0.8,$ and 1.0 samples [13]. In another case, the electrical conduction dependence on $\text{Cu}_{1-x}\text{Co}_x\text{Cr}_2\text{Se}_4$ exhibited metallic-type conductivity within the chemical $0.1 \leq x \leq 0.5$ range [16,17]. The substitution of Li by Cu in the CuCr_2Se_4 end-member caused a change from metallic to insulating behavior, which was ascribed to the suppression of holes in the ligand non-bonding p orbitals of the selenium atoms resulting from the substitution [18]. Similarly, changes occurred when chalcogen was substituted, as in $\text{CuIr}_2(\text{S}_{1-y}\text{Se}_y)_4$, with $y \leq 0.15$, as metal-insulated transition occurred along with a structural modification from a cubic to tetragonal structure. In $\text{CuCr}_2\text{S}_{4-x}\text{Se}_x$, semiconduction appeared when CuCr_2S_4 and CuCr_2Se_4 spinels were mixed with metallic conduction [19,20]. Nagata et al. reported the magnetoresistance of CuCrZrS_4 . This solid solution exhibited variable range hopping (VHR) behavior and decreasing resistivity with increasing magnetic field [21]. For other compounds, there was a progressive change in the electrical properties. $\text{Co}_{0.1}\text{Fe}_{0.9}\text{Cr}_2\text{S}_4$ showed a temperature dependence from metallic behavior (140–178 K) to semiconducting behavior at $T > 178$ K [22]. In addition, this material showed a linear decrease in electrical resistance as the applied external magnetic field increased. Chemical substitutions of Cr by Sn, such as in $\text{CuCr}_{2-x}\text{Sn}_x\text{S}_4$ ($x = 0.1$ and 0.2), resulted in p -type conduction with electrical conductivity (σ) values of approximately 1×10^3 S/m at room temperature (RT), revealing that CuCrSnS_4 exhibited semiconducting behavior with a band gap of approximately 0.9 eV [23]. In the case replacing Cr with Hf, $\text{CuCr}_{2-x}\text{Hf}_x\text{Se}_4$ exhibited metallic conduction, and the σ value increased by two orders of magnitude from $x = 0.06$ to $x = 0.14$ [24]. From the crystallographic and chemical information obtained from a single crystal sample of $\text{CuCr}_{1.1}\text{Sn}_{0.9}\text{S}_{2.3}\text{Se}_{1.7}$ a rational synthesis of a family of compounds with a chemical formula of $\text{CuCr}_{2-x}\text{Sn}_x\text{S}_{2.3}\text{Se}_{1.7}$ and $\text{CuCr}_{2-x}\text{Sn}_x\text{S}_{1.7}\text{Se}_{2.3}$ ($x = 0.4, 0.6,$ and 1.0) was carried out to study the effect of the chemical replacement of Cr by Sn and Se by S on the physical properties. The present work describes the solid-state synthesis, crystallographic and electrical properties, and density functional theory (DFT) calculations to determine the influence of the chemical substitution of tin and chalcogen on the structure and physical properties of these compounds.

2. Materials and Methods

Powder samples of $\text{CuCr}_{2-x}\text{Sn}_x\text{S}_{2.3}\text{Se}_{1.7}$ and $\text{CuCr}_{2-x}\text{Sn}_x\text{S}_{1.7}\text{Se}_{2.3}$ were prepared by directly combining high-purity elemental powders (99.99%, Aldrich) in stoichiometric amounts (~0.5 g of the compound). Firstly, powders were mixed manually in hexane with ~5wt% excess of S and Se in an agate mortar and pestle. Hexane was selected to prepare a more homogenous mixture. Then, mixed powders were pressed into disc pellets at ~10 kPa, sealed in evacuated quartz ampoules, and placed in a horizontal tubular programmable furnace. All processes were carried out in an Ar atmosphere. The ampoules were slowly heated from RT to 500 °C at a rate of 150 °C/h and maintained at this temperature for 2 h, then were heated to 850 °C at a rate of 60 °C/h and kept for 10 days. Finally, the ampoules were gradually cooled to RT at a rate of 60 °C/h. The resulting powder was annealed and pressed into a pellet, then heated at 850 °C for 7 days with a 60 °C/min heating and cooling rate to RT. A similar procedure and stoichiometric amount (~300 mg of the compound) with ~5 wt% excess of Se was used to obtain single-crystal. The ampoules were gradually cooled at 10 °C/h until RT.

Single-crystal X-ray diffraction (XRD) data for $\text{CuCr}_{1.1}\text{Sn}_{0.9}\text{S}_{2.3}\text{Se}_{1.7}$ were accumulated at 293 K with a D8 Venture Bruker AXS diffractometer equipped with Mo $K\alpha$ radiation ($\lambda = 0.71073$ Å). Data were accumulated using the Bruker SMART software package [25]. Structural refinement was performed using the SHELXL [26] and Olex2 [27] programs. Powder XRD (PXRD) patterns were collected at RT in the range of $5^\circ < 2\theta < 80^\circ$ using a Bruker

D8 Advance powder diffractometer (Bruker, Billerica, MA, USA) with Cu K α radiation ($\lambda = 1.54178 \text{ \AA}$). The XRD patterns were indexed using the CHEKCELL software [28]. The data were analyzed using Rietveld refinements performed in the MAUD program [29]. A LaB₆ powder standard was used to determine the instrumental profile. Chemical composition determination and mapping analyses of the samples were performed by energy dispersive spectroscopy (EDS) and scanning electron microscopy (SEM) using a Tescan Vega 3 scanning electron microscope equipped with a Quantax 400 EDS microanalyzer. Cylindrical pellets (6 mm in diameter and ~2 mm thick) were uniaxially pressed at approximately $5 \times 10^8 \text{ Pa}$. These samples were then mounted on double-sided carbon tape and adhered to an Al specimen holder for analysis. A Perkin–Elmer Lambda 20 UV/Vis spectrophotometer equipped with a Labsphere RSA-PE-20 diffuse reflectance accessory was used to measure the diffuse reflectance. Raman scattering measurements were conducted on a WITec alpha300 System using 532 nm wavelength excitation. The spectrometer was calibrated with a reference single-crystal Si sample (Raman peak at 520.7 cm^{-1}). The spectral data were collected at room temperature in a backscattering configuration in the spectral range of $100\text{--}450 \text{ cm}^{-1}$, with a laser spot of $\sim 1 \text{ }\mu\text{m}$ and laser power of 2 mW. The thermal analyses were performed using a Netzsch STA 449 F3 Jupiter apparatus with a heating rate of $10 \text{ K}\cdot\text{min}^{-1}$. Hall-effect measurements were performed using an ECOPIA HMS 2000 system. The pellets for electrical measurements were uniaxially pressed at approximately 2.5 tons, resulting in cylindrical pellets with a 9.00 mm diameter and thicknesses ranging from 0.93 to 1.30 mm. The Hall coefficient, $\pm 0.556 \text{ T}$, was obtained from the linear fit of the Hall resistivity. The electrical conductivity was measured using the van der Pauw method at RT. The density (ρ) was determined using the dimensions and mass of the sample, corresponding to an average pellet density of approximately 92% (experimental density/crystallographic density). Silver paint and/or InSb alloy were used as electrical contact. Electronic structure calculations were performed in the DFT framework using the Fritz Haber Institute ab initio molecular simulations (FHI-aims) package [30]. Geometry optimizations considered periodic boundary conditions with variable lattice parameters. The starting geometry was the crystallographic structure for $\text{CuCr}_{1.02}\text{Sn}_{0.98}\text{S}_{2.11}\text{Se}_{1.89}$; stoichiometry was adjusted to be close to the different systems under study. Structural relaxations considered dispersion interactions by the Tkatchenko–Scheffler approximation [31] in conjunction with the PBE density functional [32] and the ‘light’ all-electron basis set. Band structure calculations included a larger basis set (‘tight’ in FHI-aims nomenclature) and a k-grid of $2 \times 2 \times 2$ in the Self-Consistent Field step. Larger supercells (up to $8 \times 8 \times 8$) were tested but provided similar band structures to smaller $2 \times 2 \times 2$ calculations. This was expected since the unit cell was already large. Once the electron density was converged, band dispersion was plotted following the path $L \rightarrow G \rightarrow X \rightarrow W \rightarrow K$ using 50 points for each step.

3. Results and Discussion

3.1. Crystal Structure Analysis, PXRD Patterns, and SEM-EDS Analyses

The motivation for this work was to analyze how changes in the Cr/Sn and S/Se chemical substitutions influence the structure and physical properties of the CuCr_2Se_4 end-member. The crystallographic data and atomic positions of cubic $\text{CuCr}_{1.1}\text{Sn}_{0.9}\text{S}_{2.3}\text{Se}_{1.7}$ are given in Table 1 and Table S1 (see Supplementary Materials), respectively. The refinements were carried out in the $Fd\bar{3}m$ space group. The method we applied to solve the crystal structure was that of a model Cu atom occupying the tetrahedral (A) sites, and Cr and Sn cations occupying the octahedral [B] sites. This model was based on linear functions constraining the Sn, Cu, and Cr atoms at the 16d and 8a sites. The sum of the site occupation factor (SOF) was forced to equal 1 (fully occupied for $16d = (2 - x)\text{Cr} + x\text{Sn}$. Furthermore, for the chalcogenide site, the sum of the SOF was forced to equal 1 (fully occupied) for $32e = (4 - y)\text{S} + y\text{Se}$, and the Sn/Cr and S/Se atoms were also constrained to have equivalent atomic displacement parameters (ADPs).

Table 1. Crystallographic data and structure refinement details.

CuCr_{1.1}Sn_{0.9}S_{2.3}Se_{1.7} [§]	
Crystal data	
Crystal system, space group	Cubic, <i>Fd$\bar{3}m$</i>
<i>a</i> (Å)	10.3578 (15)
<i>V</i> (Å ³)	1111.2 (5)
μ (mm ⁻¹)	21.844
Crystal size (mm)	0.25 × 0.23 × 0.21
Data collection	
<i>T</i> _{min} , <i>T</i> _{min}	0.3119, 0.7485
No. of measurements	1152
<i>R</i> _{int} , <i>R</i> _σ	0.042, 0.039
No. of independent reflections	120
(sin θ / λ) _{max} (Å ⁻¹)	0.747
Refinement	
Refinement method	Full-matrix least-squares on <i>F</i> ²
No. of reflections	111
No. of parameters	10
Completeness to $\theta = 25.242^\circ$	97.6%
<i>R</i> ₁ [<i>F</i> ² > 2σ(<i>F</i> ²)], <i>R</i> ₁	0.0249, 0.0266
<i>wR</i> ₂ (<i>F</i> ²), <i>wR</i> ₂	0.0543, 0.0519
Goodness-of-fit	0.990
Extinction coefficient	0.0031 (3)
$\Delta\rho_{\max}$, $\Delta\rho_{\min}$ (e Å ⁻³)	1.32, -0.71

[§] Further details of the crystal structure investigation can be obtained from the crystallographic data with deposition number CSD 2124213. The crystallographic data can be obtained free of charge from the Cambridge Crystallographic Data Centre via http://www.ccdc.cam.ac.uk/data_request/cif.

The CuCr_{1.1}Sn_{0.9}S_{2.3}Se_{1.7} compound crystallized in a normal spinel-type structure and cell parameter *a* had an intermediate value between those of CuCrSnS₄ (10.175 Å) [33] and CuCrSnSe₄ (10.672 Å) [34], similar to the values reported for mixed spinels (Cu)_{tet}[Cr_{2-x}Sn_x]_{oct}S_{4-y}Se_y [13]. The Cu–X (X = Se/S) distance in CuCr_{1.1}Sn_{0.9}S_{2.3}Se_{1.7} was 2.3294(8) Å, which is intermediate between the Cu–Se bond length in (Cu)_{tet}[Cr_{2-x}Sn_x]_{oct}Se₄ (2.3832–2.3947 Å) and the Cu–S bond length in thiospinels (Cu)_{tet}[Ti_{1.7}M_{0.3}]_{oct}S₄ (2.2583–2.2737 Å) [5]. The Cu–X distance was near to the tetrahedral covalent radii evaluated by Pyykkö [24] for Cu–S (2.313 Å). The (Cu)X₄ tetrahedron was ideal with an angle of 109.5°. The [Cr,Sn]_{Oh}–X bond distance was 2.5403(5) Å, which is comparable to the [Cr/Sn]–Se bond length in (Cu)_{tet}[Cr_{2-x}Sn_x]_{oct}Se₄. The other important structural parameters (bond distances and angles) were as expected and were in acceptable concordance with those of other thio- and selenospinel compounds. The degree of distortion in the octahedral sites was evaluated using distortion indices published by Baur et al. [35]. The [Cr_{2-x}Sn_x]X₆ octahedron showed a ~2.0% degree of distortion, which agrees with the octahedral distortions in chalcospinels already reported in our previous research [5,6,13]. The single positional *u* parameter of the chalcogen atoms (*u*, *u*, *u*), Wyckoff position 32e, of CuCr_{1.1}Sn_{0.9}S_{2.3}Se_{1.7}, was 0.25484(4), which is comparable to the values found in cubic CuCr_{1.7}Sn_{0.3}Se₄ and CuCr_{1.5}Sn_{0.5}Se₄: *u* = 0.25663(4) and *u* = 0.25632(3), respectively [6].

From the single-crystal analysis, rational synthesis of CuCr_{2-x}Sn_xS_{2.3}Se_{1.7} and CuCr_{2-x}Sn_xS_{1.7}Se_{2.3} (*x* = 0.4, 0.6, and 1.0) powder samples were performed. The SEM backscattered electron images (mapping) and EDS measurements revealed that the chemical compositions of all the powder samples were uniform throughout the scanned region (Figure 1). For example, the experimental results determined a Cu/Cr/Sn/S/Se ratio of approximately 1.1/1.0/0.8/1.8/2.2. No secondary phases or impurity peaks were revealed within the detection limits of this technique.

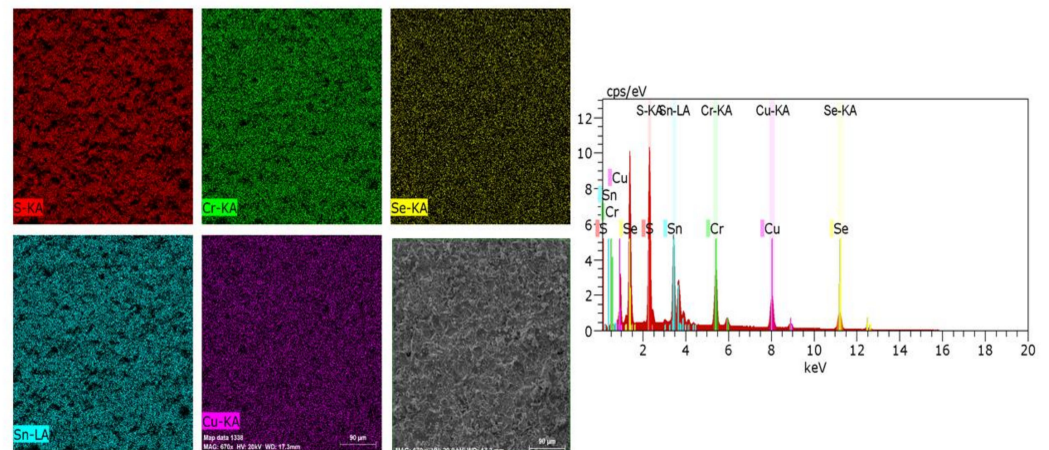


Figure 1. SEM analysis: Representative EDS mapping images (powder sample) and backscattered electron image of $\text{Cu}_{1.0}\text{Cr}_{1.0}\text{Sn}_{1.0}\text{S}_{1.7}\text{Se}_{2.3}$ (20 kV, 670 \times).

Figure 2 show the PXRD patterns of the polycrystalline materials. The sharpness of the signals indicates high crystallinity, whereas the observed interlayer spacing is in good concordance with the interplanar spacing d calculated. The entire PXRD patterns obtained for these phases were indexed to the $\text{Fd}\bar{3}m$ space group (spinel-type structure), confirming that the powder samples crystallized in a normal spinel-type structure.

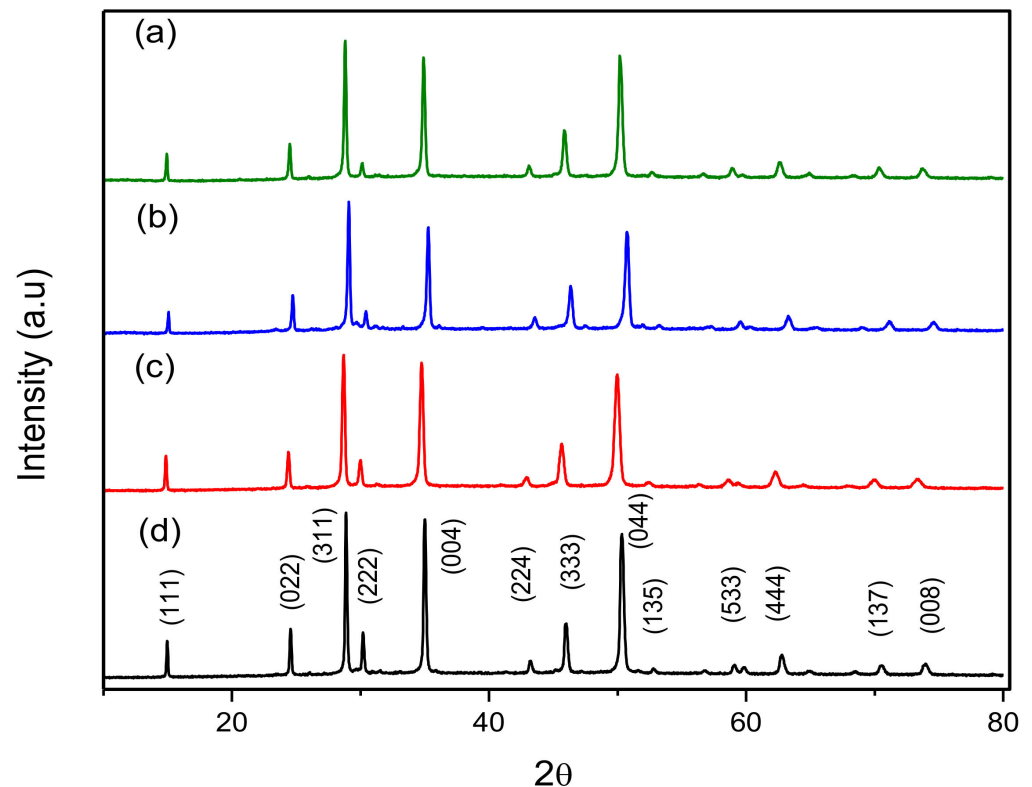


Figure 2. Representative powder XRD patterns at RT of (a) $\text{CuCr}_{1.4}\text{Sn}_{0.6}\text{S}_{2.3}\text{Se}_{1.7}$, (b) $\text{CuCr}_{1.6}\text{Sn}_{0.4}\text{S}_{2.3}\text{Se}_{1.7}$, (c) $\text{CuCr}_{1.4}\text{Sn}_{0.6}\text{S}_{1.7}\text{Se}_{2.3}$, and (d) $\text{CuCr}_{1.6}\text{Sn}_{0.4}\text{S}_{1.7}\text{Se}_{2.3}$ phases showing the corresponding hkl Miller indices.

Rietveld refinements were performed using the PXRD data collected at RT temperature (Figure S1—see Supplementary Materials). The structural model obtained was in good concordance with the model based on the single-crystal XRD data. The R-indices were

refined to reasonable values (Table 2). The Rietveld analysis refinement performed in the $\text{CuCr}_{1.6}\text{Sn}_{0.4}\text{S}_{2.3}\text{Se}_{1.7}$ sample indicated the presence of minor phase impurities. The cell lattice parameters gradually increased with increasing Sn concentration (x), which concurs with Vegard's law (Figure S2). The chemical composition of the Rietveld analysis was in accordance with the nominal compositions. As expected, $\text{CuCr}_{2-x}\text{Sn}_x\text{S}_{2.3}\text{Se}_{1.7}$ and $\text{CuCr}_{2-x}\text{Sn}_x\text{S}_{1.7}\text{Se}_{2.3}$ cell parameter phases expanded owing to the substitution of Cr [$\text{Cr}^{3+}/\text{Cr}^{4+}$] by the larger Sn^{4+} cation. The effective octahedral ionic radii of the Cr^{3+} , Cr^{4+} , and Sn^{4+} cations published by Shannon are 0.62 Å, 0.55 Å, and 0.69 Å, respectively. The cell parameter of $\text{CuCr}_{1.0}\text{Sn}_{1.0}\text{S}_{1.7}\text{Se}_{2.3}$ was larger than that of $\text{CuCr}_{1.0}\text{Sn}_{1.0}\text{S}_{2.3}\text{Se}_{1.7}$ because of the substitution of S by the larger Se anions.

Table 2. Cell a parameters and R -indices obtained from Rietveld refinement of PXRD patterns of $\text{CuCr}_{2-x}\text{Sn}_x\text{S}_{2.3}\text{Se}_{1.7}$ and $\text{CuCr}_{2-x}\text{Sn}_x\text{S}_{1.7}\text{Se}_{2.3}$ ($x = 0.4, 0.6,$ and 1.0).

	a (Å)	R_p	R_{exp}
$\text{CuCr}_{1.0}\text{Sn}_{1.0}\text{S}_{2.3}\text{Se}_{1.7}$	10.370 (2)	0.0616	0.0284
$\text{CuCr}_{1.4}\text{Sn}_{0.6}\text{S}_{2.3}\text{Se}_{1.7}$	10.240 (2)	0.0808	0.0285
$\text{CuCr}_{1.6}\text{Sn}_{0.4}\text{S}_{2.3}\text{Se}_{1.7}$	10.180 (3)	0.1254	0.0471
$\text{CuCr}_{1.0}\text{Sn}_{1.0}\text{S}_{1.7}\text{Se}_{2.3}$	10.447 (2)	0.1040	0.0283
$\text{CuCr}_{1.4}\text{Sn}_{0.6}\text{S}_{1.7}\text{Se}_{2.3}$	10.322 (1)	0.0755	0.0266
$\text{CuCr}_{1.6}\text{Sn}_{0.4}\text{S}_{1.7}\text{Se}_{2.3}$	10.250 (1)	0.0691	0.0261

3.2. Electrical and Optical Properties, Raman Scattering and DFT Calculations

The conductivity, mobility, magnetoresistance, and carrier concentrations were measured using the van der Pauw method. Room-temperature Hall-effect measurements were conducted with a magnetic field intensity of 0.556 T and a current of 0.5 mA. The measured conductivity, mobility, carrier concentration, and magnetoresistance values are listed in Table 3.

Table 3. Transport properties obtained from Hall-effect measurements of $\text{CuCr}_{2-x}\text{Sn}_x\text{S}_{2.3}\text{Se}_{1.7}$ and $\text{CuCr}_{2-x}\text{Sn}_x\text{S}_{1.7}\text{Se}_{2.3}$.

	Conductivity (S/cm)	Carrier Concentration (cm^{-3})	Mobility ($\text{cm}^2/\text{V}\cdot\text{s}$)	Magneto-Resistance (Ω)
$\text{CuCr}_{1.0}\text{Sn}_{1.0}\text{S}_2\text{Se}_2$	1.11×10^{-1}	$+1.58 \times 10^{20}$	9.13×10^{-3}	6.70×10^{-3}
$\text{CuCr}_{1.4}\text{Sn}_{0.6}\text{S}_{2.3}\text{Se}_{1.7}$	23.9	$+1.90 \times 10^{20}$	7.86×10^{-1}	3.89×10^{-4}
$\text{CuCr}_{1.6}\text{Sn}_{0.4}\text{S}_{2.3}\text{Se}_{1.7}$	10.7	$+5.30 \times 10^{19}$	1.89	5.45×10^{-4}
$\text{CuCr}_{1.4}\text{Sn}_{0.6}\text{S}_{1.7}\text{Se}_{2.3}$	9.04	$+3.48 \times 10^{20}$	2.53×10^{-1}	4.11×10^{-4}
$\text{CuCr}_{1.6}\text{Sn}_{0.4}\text{S}_{1.7}\text{Se}_{2.3}$	17.2	$+6.11 \times 10^{20}$	2.18×10^{-1}	3.69×10^{-4}

All the $\text{CuCr}_{2-x}\text{Sn}_x\text{S}_{2.3}\text{Se}_{1.7}$ and $\text{CuCr}_{2-x}\text{Sn}_x\text{S}_{1.7}\text{Se}_{2.3}$ ($x = 0.4, 0.6,$ and 1.0) samples showed p-type conductivity, which was consistent with the results reported for $\text{CuCr}_{2-x}\text{Sn}_x\text{S}_4$ and $\text{CuCr}_{2-x}\text{Sb}_x\text{S}_4$ [23,36]. The temperature dependence electrical conductivity for $\text{CuCr}_{1.4}\text{Sn}_{0.6}\text{S}_{1.7}\text{Se}_{2.3}$ and $\text{CuCr}_{1.6}\text{Sn}_{0.4}\text{S}_{1.7}\text{Se}_{2.3}$ is shown in Figure S3. The electrical conductivity (σ) increased almost exponentially with increasing temperature, revealing semiconductor behavior for the sample, followed by a temperature dependence of $\sigma \sim T^n$. The Hall coefficients were positive at RT, which is indicative of p-type behavior. The hole concentrations were similar at all studied phases, with a carrier concentration of approximately 10^{20} cm^{-3} . Khan et al. reported values of approximately $2.41 \times 10^{21} \text{ cm}^{-3}$ for $\text{CuCr}_{1.5}\text{Sb}_{0.5}\text{S}_4$, which showed typical degenerate semiconductor behavior. Electrical mobility is an important property for evaluating electrical behavior. The electrical hole mobilities of $\text{CuCr}_{2-x}\text{Sn}_x\text{S}_{2.3}\text{Se}_{1.7}$ and $\text{CuCr}_{2-x}\text{Sn}_x\text{S}_{1.7}\text{Se}_{2.3}$ ($\sim 0.10 \text{ cm}^2/\text{V}\cdot\text{s}$) were smaller than the value reported for $\text{CuCr}_{1.5}\text{Sb}_{0.5}\text{S}_4$ ($4.06 \text{ cm}^2/\text{V}\cdot\text{s}$). The chalcogen S/Se substitution thus led to low mobility. The electrical conductivities, σ , of the $\text{CuCr}_{1.0}\text{Sn}_{1.0}\text{S}_2\text{Se}_2$, $\text{CuCr}_{2-x}\text{Sn}_x\text{S}_{2.3}\text{Se}_{1.7}$, and $\text{CuCr}_{2-x}\text{Sn}_x\text{S}_{1.7}\text{Se}_{2.3}$ phases were lower than those of the CuCr_2Se_4 (667 S/cm) and CuCr_2S_4 (1110 S/cm) end-members. This

indicates that σ is quite sensitive to the Sn content. The electrical conductivity σ showed chromium-content dependence, and it increased in all cases with decreasing x values. The only exception was the $\text{CuCr}_{1.6}\text{Sn}_{0.4}\text{S}_{2.3}\text{Se}_{1.7}$ sample, which had the lowest σ value. This sample showed a complex chemical composition related to chromium content; the Rietveld analysis refinement performed for this sample indicated the presence of minor phase impurities. Therefore, such as inhomogeneity could be responsible for the exceptional conductivity values. On the other hand, the σ value for $\text{CuCr}_{1.6}\text{Sn}_{0.4}\text{S}_{1.7}\text{Se}_{2.3}$ was approximately 2 times larger than the value obtained for $\text{CuCr}_{1.4}\text{Sn}_{0.6}\text{S}_{1.7}\text{Se}_{2.3}$ and approximately 80 times larger than that of $\text{CuCr}_{1.0}\text{Sn}_{1.0}\text{S}_{2.0}\text{Se}_{2.0}$. This suggests that the chromium content is the main reason for the increased conductivity in these systems. Similar results have been observed for $\text{CuCr}_{1.1}\text{Sn}_{0.9}\text{S}_4$ (~ 5.0 S/cm) and $\text{CuCr}_{1.2}\text{Sn}_{0.8}\text{S}_4$ (~ 40 S/cm) thiospinels [23]. Nagata et al. reported large magnetoresistance in CuCrZrS_4 . In this phase, the chromium site was partially substituted by a diamagnetic metal. This solid solution exhibited VRH behavior and resistivity that decreased with an increasing magnetic field [21]. In our systems, very low magnetoresistance was observed at an applied magnetic field of 0.556 T (see Table 3). This suggests that the electronic transport properties of CuCrMX_4 thio- and selenospinel are highly sensitive to chemical substitution.

These materials showed behavior typical of semiconductors, and the band gaps were measured using UV-vis-IR NIR diffuse reflectance spectroscopy (Figure 3). The observed band gaps of $\text{CuCr}_{2-x}\text{Sn}_x\text{S}_{2.3}\text{Se}_{1.7}$ and $\text{CuCr}_{2-x}\text{Sn}_x\text{S}_{1.7}\text{Se}_{2.3}$ ranged from ~ 1.6 to 1.9 eV. These values are comparable to those observed for CoCr_2S_4 nanocrystals (1.7 eV) and CuCr_2Se_4 (~ 2.0 eV) [37,38].

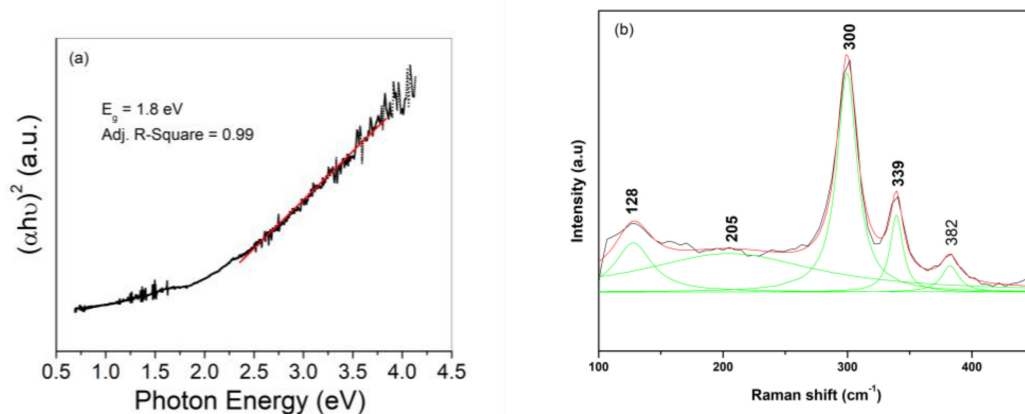


Figure 3. (a) Representative plot of diffuse reflectance against photon energy ($h\nu$) for $\text{CuCr}_{1.0}\text{Sn}_{1.0}\text{S}_{2.3}\text{Se}_{1.7}$ sample. Red line is included to show the baseline, and linear extrapolation used to determine the band gap. (b) Representative Raman spectral of $\text{CuCr}_{1.6}\text{Sn}_{0.4}\text{S}_{2.3}\text{Se}_{1.7}$ powder sample with the different contributions deduced from the fitting of the different peaks with Lorentzian curves (green lines).

Raman spectra of the $\text{CuCr}_{2-x}\text{Sn}_x\text{S}_{2.3}\text{Se}_{1.7}$ and $\text{CuCr}_{2-x}\text{Sn}_x\text{S}_{1.7}\text{Se}_{2.3}$ materials were compiled inside the 100 to 450 cm^{-1} range (Figure 3). The spectra present five signals at approximately ~ 124 , 203, 265, 295, and 350 cm^{-1} . These signals are equivalent to the $(\text{Cu})_{\text{tet}}[\text{Cr}_{2-x}\text{Sn}_x]_{\text{oct}}\text{S}_2\text{Se}_2$ ($0.2 \leq x \leq 1.0$) spinels, where a partial substitution of Cr by Sn occurs [12]. The frequencies and vibrational assignment of Raman bands with respect to the CuCrSnS_4 and $(\text{Cu})_{\text{tet}}[\text{Cr}_{2-x}\text{Sn}_x]_{\text{oct}}\text{S}_2\text{Se}_2$ is shown in Table S2 (see Supplementary Materials). The signals at ~ 350 cm^{-1} and ~ 270 cm^{-1} have been assigned to the A_{1g} and F_{2g} (2) modes which are associated with symmetrical and asymmetrical stretching of the chalcogen bond in the tetrahedral metal, respectively. We observed a significant shift at lower frequencies for peaks at ~ 350 cm^{-1} , 295 cm^{-1} , and ~ 265 cm^{-1} . The displacement of the signal is attributed to the incorporation of Sn atoms in an octahedral position. The greater weight of Sn than Cr leads to a shift towards lower energies. On the

other hand, as Sn–chalcogen interactions influence the environment, this results in a change in the polarities of the bonds inducing variations in the intensity and position of the signals.

To rationalize the physical measurements, DFT calculations were carried out on compounds with different elemental compositions. To reach the stoichiometry of the current compounds under discussion, the structure of the CuCr_2Se_4 spinel was modified to account for the different Cr/Sn and S/Se ratios. Ions were placed randomly, and geometric optimization was repeated for three different ion arrangements for each case. To avoid the optimization of large supercells, model stoichiometries were chosen to be close to the studied systems while maintaining a single unit cell. Optimized cell parameters agreed with the experimental data (less than 2% deviation in cell length) and are presented in Table 4. Deviation between repetitions of the same stoichiometry (σ) was low, indicating that the results were robust.

Table 4. Experimental and calculated cell parameters for different $\text{CuCr}_{2-x}\text{Sn}_x\text{S}_{4-y}\text{Se}_y$ compounds. The standard deviation was calculated from three optimizations with the same stichometry but different ion arrangements.

Model Stoichiometry	Reference Formula	<i>a</i> Exp (Å)	<i>a</i> Calc (Å)	σ
$\text{Cu}_8\text{Cr}_8\text{Sn}_8\text{S}_{16}\text{Se}_{16}$	$\text{Cu}_1\text{Cr}_1\text{Sn}_1\text{S}_2\text{Se}_2$	10.398 [§]	10.521	0.0197
$\text{Cu}_8\text{Cr}_8\text{Sn}_8\text{S}_{19}\text{Se}_{13}$	$\text{Cu}_1\text{Cr}_1\text{Sn}_1\text{S}_{2.3}\text{Se}_{1.7}$	10.370	10.465	0.0195
$\text{Cu}_8\text{Cr}_{11}\text{Sn}_5\text{S}_{13}\text{Se}_{19}$	$\text{Cu}_1\text{Cr}_{1.4}\text{Sn}_{0.6}\text{S}_{1.7}\text{Se}_{2.3}$	10.322	10.413	0.0170
$\text{Cu}_8\text{Cr}_{11}\text{Sn}_5\text{S}_{19}\text{Se}_{13}$	$\text{Cu}_1\text{Cr}_{1.4}\text{Sn}_{0.6}\text{S}_{2.3}\text{Se}_{1.7}$	10.24	10.307	0.0155
$\text{Cu}_8\text{Cr}_{13}\text{Sn}_3\text{S}_{13}\text{Se}_{19}$	$\text{Cu}_1\text{Cr}_{1.6}\text{Sn}_{0.4}\text{S}_{1.7}\text{Se}_{2.3}$	10.25	10.277	0.0499
$\text{Cu}_8\text{Cr}_{13}\text{Sn}_3\text{S}_{19}\text{Se}_{13}$	$\text{Cu}_1\text{Cr}_{1.6}\text{Sn}_{0.4}\text{S}_{2.3}\text{Se}_{1.7}$	10.18	10.197	0.0100

[§] cell *a* parameter obtained from single-crystal analysis of $\text{CuCr}_{1.0}\text{Sn}_{1.0}\text{S}_{2.1}\text{Se}_{1.9}$ was 10.398(2) Å [12].

Regarding the electronic structure of the different spinels, the Cr centers concentrated most of the spin density; Mulliken spin populations were always around 3.2–3.3 electrons. A smaller spin polarization featuring the opposite spin was observed for S/Se atoms. Cu ions showed small spin polarization, suggesting a monovalent state for this ion. The different models showed minor changes, as the electronic configuration did not change qualitatively when the elemental composition was modified. The calculated magnetic moment was consistent with the presence of monovalent Cu ions and Cr^{III} ($S = 3/2$) centers coupled antiferromagnetically with a delocalized electron with relevant spin density at the S/Se atoms. This picture is in line with neutron diffraction measurements of CuCr_2Se_4 performed by Colominas [38]. Band structures for all models were consistent with the observed semiconductor behavior and presented noticeable spin polarization (Figure S4). The density of states clearly reflected the spin configuration of the systems. Figure 4 present the element and spin-resolved DOS for $\text{Cu}_8\text{Cr}_8\text{Sn}_8\text{S}_{16}\text{Se}_{16}$. The unpaired electrons associated with the Cr^{III} ion appear as a large contribution in the upper part of the valence band between -6 and -7 eV. Unoccupied beta d-orbitals appear as a broad peak ranging from -5.5 eV to -2.5 eV. The unpaired electron from S/Se is connected with the larger contribution of these ions in the occupied part of the beta density of states. Other models feature similar DOS plots (shown as Figure S5 in SI).

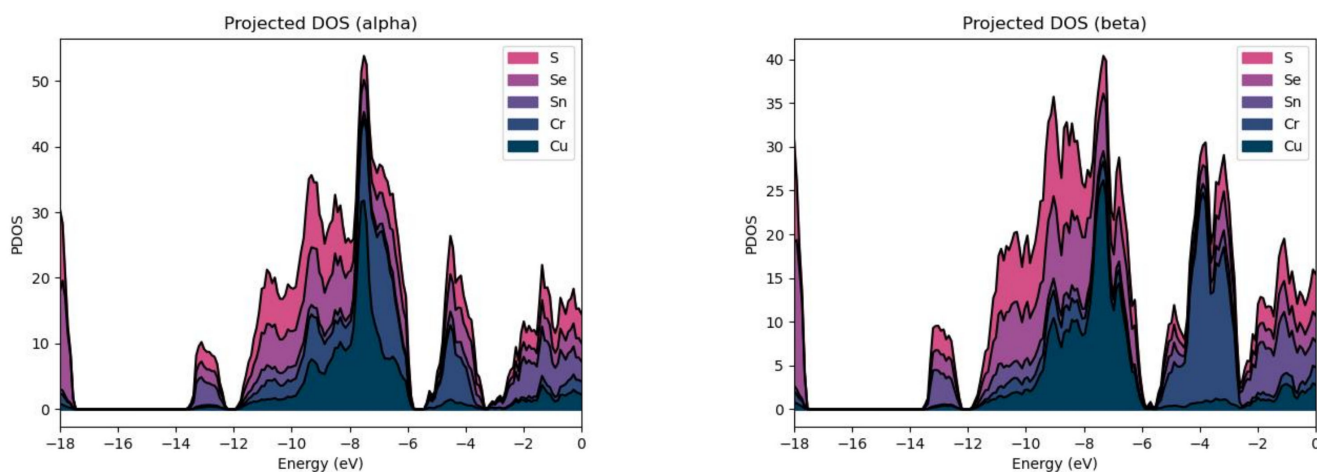


Figure 4. Element and spin-resolved density of states for the model $\text{CuCrSnS}_2\text{Se}_2$. Remaining systems are presented in Figure S5.

4. Conclusions

Single-crystal $\text{CuCr}_{1.1}\text{Sn}_{0.9}\text{S}_{2.3}\text{Se}_{1.7}$ and powder samples of $\text{CuCr}_{2-x}\text{Sn}_x\text{S}_{2.3}\text{Se}_{1.7}$ and $\text{CuCr}_{2-x}\text{Sn}_x\text{S}_{1.7}\text{Se}_{2.3}$ ($x = 0.4, 0.6,$ and 1.0) were obtained via using conventional solid-state synthesis. Their crystal structures, as determined by single-crystal XRD, corresponded to normal spinel-type structures. For all the samples, the vibrational analysis and optical properties were in good agreement with the selenospinel phases. The electrical measurements showed a *p*-type semiconductor behavior and electrical conductivities lower than those of the seleno- and sulfospinel CuCr_2X_4 . DFT calculations suggested copper ions are monovalent and hence, diamagnetic. The spin density concentrated in the Cr^{III} ions ($S = 3/2$), while a more delocalized contribution was associated with S/Se. The theoretical DFT and experimental measurements clearly demonstrated that the conductivity is quite sensitive to the Sn content. However, the non-stoichiometry in the chalcogen, in this case, selenium and sulfur, had a weak influence on the electrical properties.

Supplementary Materials: The following materials are available online at <https://www.mdpi.com/article/10.3390/app12031586/s1>. Table S1: Fractional atomic coordinates and isotropic or equivalent isotropic displacement parameters; Figure S1: Representative powder XRD data for $\text{CuCr}_{1.0}\text{Sn}_{1.0}\text{S}_{2.3}\text{Se}_{1.7}$; Figure S2: Vegard's Law; Figure S3: Electrical conductivity against temperature of $\text{CuCr}_{2-x}\text{Sn}_x\text{S}_{2.3}\text{Se}_{1.7}$; Figure S4: Band structures for calculated models. Alpha bands are depicted in black, and beta bands are presented in green; Figure S5: Element and spin-resolved density of states for all calculated systems.

Author Contributions: Conceptualization, A.G. and S.M.; methodology and experiments, P.V.-G., P.B., A.G. and S.M.; writing—original draft preparation, S.M., P.V.-G., D.A. and A.G.; electrical measurements, A.G. and P.V.-G.; DFT Calculations, D.A. All authors have read and agreed to the final version of the manuscript.

Funding: This research received no external funding.

Institutional Review Board Statement: Not applicable.

Informed Consent Statement: Not applicable.

Data Availability Statement: Not applicable.

Acknowledgments: This work was supported by the Chilean-French International Associated Laboratory for 'Multifunctional Molecules and Materials' (LIAM3-CNRS N°1027). The authors also thank FONDEQUIP grant EQM140142 for Raman Witec Alpha 300 equipment and the Unidad de Equipamiento Científico "MAINI-UCN" of the Universidad Católica del Norte for the generation of diffuse reflectance spectroscopy data through the FONDEQUIP UV-VIS-NIR grant EQM160120.

I (A.G.) am also deeply grateful for the scientific collaboration, friendliness, and willingness of Professors Carlos Pico and María Luisa Veiga to support me in an unselfish disposition.

Conflicts of Interest: The authors declare no conflict of interest.

References

1. Ramirez, A.P.; Cava, R.J.; Krajewski, J. Colossal magnetoresistance in Cr-based chalcogenide spinels. *Nature* **1997**, *386*, 156–159. [[CrossRef](#)]
2. Krohns, S.; Schrettle, F.; Lunkenheimer, P.; Tsurkan, V.; Loidl, A. Colossal magnetocapacitive effect in differently synthesized and doped CdCr_2S_4 . *Phys. B Condens. Matter* **2008**, *403*, 4224–4227. [[CrossRef](#)]
3. Fujimoto, Y.; Fujita, T.; Mitsudo, S.; Idehara, T.; Kawashima, Y.; Nagata, S. High-frequency ESR studies of colossal magnetoresistance system $\text{Cu}(\text{Cr}_{1-x}\text{Zr}_x)_2\text{S}_4$. *J. Magn. Magn. Mater.* **2007**, *310*, 1991–1993. [[CrossRef](#)]
4. Ozel, F.; Kılıc, H.S.; Coskun, H.; Devci, I.; Sarilmaz, A.; Balıkcıoğlu, A.; Gundogdu, Y.; Aljabour, A.; Ozen, A.; Gezgin, S.Y.; et al. A general review on the thiospinels and their energy applications. *Mater. Today Energy* **2021**, *21*, 100822. [[CrossRef](#)]
5. Barahona, P.; Galdámez, A.; López-Vergara, F.; Manríquez, V.; Peña, O. Crystal structure and magnetic properties of titanium-based $\text{CuTi}_{2-x}\text{M}_x\text{S}_4$ and $\text{CuCr}_{2-x}\text{Ti}_x\text{Se}_4$ chalcospinels. *J. Solid State Chem.* **2014**, *212*, 114–120. [[CrossRef](#)]
6. Pinto, C.; Galdámez, A.; Barahona, P.; Moris, S.; Peña, O. Crystal structure, Raman scattering and magnetic properties of $\text{CuCr}_{2-x}\text{Zr}_x\text{Se}_4$ and $\text{CuCr}_{2-x}\text{Sn}_x\text{Se}_4$ selenospinels. *J. Magn. Magn. Mater.* **2018**, *456*, 160–166. [[CrossRef](#)]
7. Valencia-Gálvez, P.; Peña, O.; Moris, S.; Barahona, P. Raman characterization of $\text{CuCr}_{2-x}\text{Sn}_x\text{S}_4$ spinels. *J. Chil. Chem. Soc.* **2019**, *64*, 4285–4289. [[CrossRef](#)]
8. Moris, S.; Barahona, P.; Galdámez, A. Crystal structure of $(\text{Cu}_{0.51}\text{In}_{0.49})_{\text{tet}}[\text{Cr}_{1.74}\text{In}_{0.26}]_{\text{oct}}\text{Se}_4$ selenospinel, $\text{Cu}_{0.51}\text{In}_{0.75}\text{Cr}_{1.74}\text{Se}_4$. *Z. Kristallogr. NCS* **2019**, *234*, 421–422. [[CrossRef](#)]
9. Sickafus, K.E.; Wills, J.M.; Grimes, N.W. Structure of Spinel. *J. Am. Ceram. Soc.* **1999**, *82*, 3279–3292. [[CrossRef](#)]
10. Biagioni, C.; Pasero, M. The systematics of the spinel-type minerals: An overview. *Am. Mineral.* **2014**, *99*, 1254–1264. [[CrossRef](#)]
11. Iijima, Y.; Kamei, Y.; Kobayashi, N.; Awaka, J.; Iwasa, T.; Ebisu, S.; Chikazawa, S.; Nagata, S. A new ferromagnetic thiospinel CuCrZrS_4 with re-entrant spin-glass behaviour. *Philos. Mag.* **2003**, *83*, 2521–2530. [[CrossRef](#)]
12. Moris, S.; Valencia-Gálvez, P.; Mejía-López, J.; Peña, O.; Barahona, P.; Galdámez, A. $(\text{Cu})_{\text{tet}}(\text{Cr}_{2-x}\text{Sn}_x)_{\text{oct}}\text{S}_{4-y}\text{Se}_y$ Spinels: Crystal Structure, Density Functional Theory Calculations, and Magnetic Behavior. *Inorg. Chem.* **2019**, *58*, 13945–13952. [[CrossRef](#)] [[PubMed](#)]
13. Kimura, A.; Matsuno, J.; Okabayashi, J.; Fujimori, A.; Shishidou, T.; Kulatov, E.; Kanomata, T. Soft X-ray magnetic circular dichroism study of the ferromagnetic spinel-type Cr chalcogenides. *Phys. Rev. B* **2001**, *63*, 224420. [[CrossRef](#)]
14. Lotgering, F.K. Ferromagnetism in spinels: CuCr_2S_4 and CuCr_2Se_4 . *Solid State Commun.* **1964**, *2*, 55–56. [[CrossRef](#)]
15. Kariya, F.; Ebisu, S.; Nagata, S. Evolution from a ferromagnetic to a spin-glass regime in the spinel-type $\text{Cu}(\text{Cr}_{1-x}\text{Ti}_x)_2\text{S}_4$. *J. Solid State Chem.* **2009**, *182*, 608–616. [[CrossRef](#)]
16. Maciążek, E.; Molak, A.; Goryczka, T. Influence of cobalt substitution on structure and electric conduction of CuCr_2Se_4 . *J. Alloy. Compd.* **2007**, *441*, 222–230. [[CrossRef](#)]
17. Gogowicz, M.; Juszczyk, S.; Warczewski, J.; Mydlarz, T. Ferrimagnetism of $\text{Cu}_{0.45}\text{Co}_{0.55}\text{Cr}_2\text{S}_{4-y}\text{Se}_y$. *Phys. Rev. B* **1987**, *35*, 7073–7080. [[CrossRef](#)]
18. Li, R.; Qu, Z.; Zhang, L.; Ling, L.; Tong, W.; Zhang, Y. Structure, magnetic and transport properties of Li-doped CuCr_2Se_4 . *Solid State Commun.* **2010**, *150*, 2289–2293. [[CrossRef](#)]
19. Koroleva, L.I. Antiferromagnetic states of charge carriers in the ferromagnetic semiconductors $\text{CuCr}_2\text{S}_{4-x}\text{Se}_x$ ($0.5 < x < 1.5$) with Curie points above room temperature. *J. Exp. Theor. Phys.* **1994**, *79*, 153–162.
20. Tsuji, S.; Kumagai, K.; Matsumoto, N.; Nagata, S. Metal-insulator transition in the spinel $\text{CuIr}_2(\text{S}_{1-x}\text{Se}_x)_4$ system studied by NMR. *Phys. C Supercond. Its Appl.* **1997**, *282*, 1107–1108. [[CrossRef](#)]
21. Furubayashi, T.; Suzuki, H.; Kobayashi, N.; Nagata, S. Large negative magnetoresistance in thiospinel CuCrZrS_4 . *Solid State Commun.* **2004**, *131*, 505–508. [[CrossRef](#)]
22. Kim, S.J.; Kim, W.C.; Sur, J.C.; Kim, C.S. Magnetic and electron transport properties in $\text{Co}_{0.1}\text{Fe}_{0.9}\text{Cr}_2\text{S}_4$. *J. Magn. Magn. Mater.* **2002**, *239*, 100–102. [[CrossRef](#)]
23. Bourges, C.; Srinivasan, B.; Fontaine, B.; Sauerschnig, P.; Minard, A.; Halet, J.F.; Miyazaki, Y.; Berthebaud, D.; Mori, T. Tailoring the thermoelectric and structural properties of Cu-Sn based thiospinel compounds $[\text{CuM}_{1+x}\text{Sn}_{1-x}\text{S}_4 (\text{M} = \text{Ti, V, Cr, Co})]$. *J. Mater. Chem. C* **2020**, *8*, 16368–16383. [[CrossRef](#)]
24. Maciążek, E.; Malicka, E.; Gagor, A.; Stokłosa, Z.; Groń, T.; Sawicki, B.; Duda, H.; Gudwański, A. Semiconducting-metallic transition of singlecrystalline ferromagnetic Hf-doped CuCr_2Se_4 spinels. *Phys. B Condens. Matter* **2017**, *520*, 116–122. [[CrossRef](#)]
25. Bruker Analytical X-ray Instruments Inc. SMART, SAINTPLUS V6.02, SHELXTL V6.10 and SADABS; Bruker Analytical X-ray Instruments Inc.: Madison, WI, USA, 2015.
26. Sheldrick, G.M.; SHELXL-97. *Program for the Refinement of Crystal Structures*; University of Göttingen: Stuttgart, Germany; Göttingen, Germany, 1997.
27. Dolomanov, O.V.; Bourhis, L.J.; Gildea, R.J.; Howard, J.A.K.; Puschmann, H. OLEX2: A complete structure solution, refinement and analysis program. *J. Appl. Crystallogr.* **2009**, *42*, 339–341. [[CrossRef](#)]

28. Jean Laugier et Bernard Bochu. CHEKCELL, Développé at Laboratoire des Matériaux et du Génie Physique Ecole Nationale Supérieure de Physique de Grenoble (INPG) Domaine Universitaire BP 46, 38402 Saint Martin d'Hères France. Available online: <http://www.ccp14.ac.uk/tutorial/lmgp/> (accessed on 1 September 2021).
29. Lutterotti, L. Total pattern fitting for the combined size–strain–stress–texture determination in thin film diffraction. *Nucl. Inst. Methods Phys. Res. B* **2010**, *268*, 334–340. [[CrossRef](#)]
30. Blum, V.; Gehrke, R.; Hanke, F.; Havu, P.; Havu, V.; Ren, X.; Reuter, K.; Scheffler, M. Ab initio molecular simulations with numeric atom-centered orbitals. *Comput. Phys. Commun.* **2009**, *180*, 2175–2196. [[CrossRef](#)]
31. Tkatchenko, A.; Scheffler, M. Accurate Molecular Van Der Waals Interactions from Ground-State Electron Density and Free-Atom Reference Data. *Phys. Rev. Lett.* **2009**, *102*, 73005. [[CrossRef](#)]
32. Perdew, J.P.; Burke, K.; Ernzerhof, M. Generalized Gradient Approximation Made Simple. *Phys. Rev. Lett.* **1996**, *77*, 3865–3868. [[CrossRef](#)]
33. Riedel, E.; Morlock, W. Spinelle mit substituierten Nichtmetallteilgittern VI Röntgenographische und elektronische Eigenschaften, Mößbauer- und IR-Spektren des Spinellsystems $\text{CuCrSn}(\text{S}_{1-x}\text{Se}_x)_4$. *Z. Anorg. Allg. Chem.* **1978**, *438*, 233–241. [[CrossRef](#)]
34. Mähl, D.; Pickardt, J.; Reuter, B. Züchtung und Untersuchung von Einkristallen der Verbindungen CuCrZrSe_4 und CuCrSnSe_4 . *Z. Anorg. Allg. Chem.* **1984**, *508*, 197–200. [[CrossRef](#)]
35. Pyykkö, P. Refitted tetrahedral covalent radii for solids. *Phys. Rev. B* **2012**, *85*, 024115. [[CrossRef](#)]
36. Khan, A.U.; Al Orabi, R.A.R.; Pakdel, A.; Vaney, J.B.; Fontaine, B.; Gautier, R.; Halet, J.F.; Mitani, S.; Mori, T. Sb Doping of Metallic CuCr_2S_4 as a Route to Highly Improved Thermoelectric Properties. *Chem. Mater.* **2017**, *29*, 2988–2996. [[CrossRef](#)]
37. Ramasamy, K.; Sims, H.; Gupta, R.K.; Kumar, D.; Butler, W.H.; Gupta, A. $\text{Co}_x\text{Cu}_{1-x}\text{Cr}_2\text{S}_4$ Nanocrystals: Synthesis, Magnetism, and Band Structure Calculations. *Chem. Mater.* **2013**, *25*, 4003–4009. [[CrossRef](#)]
38. Colominas, C. Neutron-Diffraction Investigation of CuCr_2Se_4 and CuCr_2Te_4 . *Phys. Rev.* **1967**, *153*, 558–560. [[CrossRef](#)]